nanomaterials

MDPI

Article

Monolithic Integration of Semi-Transparent and Flexible Integrated Image Sensor Array with a-IGZO Thin-Film Transistors (TFTs) and p-i-n Hydrogenated Amorphous Silicon Photodiodes

Donghyeong Choi [1,2,†], Ji-Woo Seo [1,2,†], Jongwon Yoon [1], Seung Min Yu [3], Jung-Dae Kwon [1], Seoung-Ki Lee [2,*] and Yonghun Kim [1,*]

[1] Department of Energy and Electronic Materials, Surface Nano Materials Division, Korea Institute of Materials Science (KIMS), Changwon 51508, Republic of Korea; baru2300@kims.re.kr (D.C.); wldn0816@kims.re.kr (J.-W.S.); jwyoon@kims.re.kr (J.Y.); jdkwon@kims.re.kr (J.-D.K.)
[2] School of Materials Science and Engineering, Pusan National University, Busan 46241, Republic of Korea
[3] Analytical Research Division, Korea Basic Science Institute, Jeonju 54907, Republic of Korea; smyu0409@kbsi.re.kr
* Correspondence: ifriend@pusan.ac.kr (S.-K.L.); kyhun09@kims.re.kr (Y.K.)
† These authors contributed equally to this work.

Abstract: A novel approach to fabricating a transparent and flexible one-transistor–one-diode (1T-1D) image sensor array on a flexible colorless polyimide (CPI) film substrate is successfully demonstrated with laser lift-off (LLO) techniques. Leveraging transparent indium tin oxide (ITO) electrodes and amorphous indium gallium zinc oxide (a-IGZO) channel-based thin-film transistor (TFT) backplanes, vertically stacked p-i-n hydrogenated amorphous silicon (a-Si:H) photodiodes (PDs) utilizing a low-temperature (<90 °C) deposition process are integrated with a densely packed 14 × 14 pixel array. The low-temperature-processed a-Si:H photodiodes show reasonable performance with responsivity and detectivity for 31.43 mA/W and 3.0 × 10^{10} Jones (biased at −1 V) at a wavelength of 470 nm, respectively. The good mechanical durability and robustness of the flexible image sensor arrays enable them to be attached to a curved surface with bending radii of 20, 15, 10, and 5 mm and 1000 bending cycles, respectively. These studies show the significant promise of utilizing highly flexible and rollable active-matrix technology for the purpose of dynamically sensing optical signals in spatial applications.

Keywords: oxide TFT; a-IGZO; a-Si:H; photodiode; image sensor; flexible; transparent; low-temperature process

check for updates

Citation: Choi, D.; Seo, J.-W.; Yoon, J.; Yu, S.M.; Kwon, J.-D.; Lee, S.-K.; Kim, Y. Monolithic Integration of Semi-Transparent and Flexible Integrated Image Sensor Array with a-IGZO Thin-Film Transistors (TFTs) and p-i-n Hydrogenated Amorphous Silicon Photodiodes. *Nanomaterials* **2023**, *13*, 2886. https://doi.org/10.3390/nano13212886

Academic Editor: Marco Cannas

Received: 10 September 2023
Revised: 12 October 2023
Accepted: 27 October 2023
Published: 31 October 2023

Copyright: © 2023 by the authors. Licensee MDPI, Basel, Switzerland. This article is an open access article distributed under the terms and conditions of the Creative Commons Attribution (CC BY) license (https://creativecommons.org/licenses/by/4.0/).

1. Introduction

The field of transparent and high-performance thin-film transistors (TFTs) has witnessed remarkable advancements, with amorphous indium–gallium-zinc oxide (a-IGZO) thin-film transistors emerging as a promising material [1–7]. These TFTs exhibit exceptional field-effect mobility, along with impressive on/off switching exceeding 10^8 [8,9]. Such attributes have positioned them as compelling candidates for cutting-edge applications in flat-panel displays and imagers [10–12].

Notably, the integration of a-IGZO TFTs with organic light-emitting diodes (OLEDs) has facilitated the development of transparent and efficient display technologies [13–16]. Furthermore, coupling a-IGZO TFTs with perovskite materials has paved the way for high-performance image sensors [17–19]. Also, there is a current surge in research focused on the advancement of photodiodes utilizing organic materials [20]. This combination underscores the versatility and potential of a-IGZO TFTs in diverse transparent and flexible optoelectronic applications. In contrast to conventional amorphous silicon TFTs, oxide

TFTs offer significant advantages for the development of high-performance image sensors. They boast superior on/off ratios and frame rates, enabling the realization of advanced image-capturing capabilities [21]. Furthermore, the use of transparent conductive oxide (TCO) materials like indium tin oxide (ITO) for both gates and bottom-top electrodes has enabled the fabrication of all-transparent TFTs [22,23]. This innovation not only ensures low voltage and power consumption but also enhances energy efficiency, rendering these devices particularly attractive for integration into smart devices, in-car displays, and wearable electronics [24–27]. Also, a blue light detector can be typically used for blue light hazards [28]. It prominently functions at 470 nm, making it suitable for use as an image sensor. This capability positions it for applications in areas such as cameras, where imaging sensing is required [29]. To achieve a transparent image sensor and enhanced flexibility, the utilization of a colorless polyimide (CPI) substrate has been employed, effectively minimizing the curvature radius [30]. This strategic implementation addresses the need for improved flexibility while ensuring optimal performance in the context of the advanced optical materials domain [31]. However, most transparent and flexible image sensor arrays are limited to photolithographic patterning and the large spatial uniformity of photodiodes, such as perovskite and organic-based photosensing materials. In this regard, hydrogenated amorphous silicon-based (a-Si:H) photodiodes (PDs) exhibit a remarkable combination of exceptional performance and cost-effectiveness [32]. Their high efficiency, coupled with reasonable production costs, has contributed to their recognition in various optoelectronic applications. These a-Si:H photodiodes are characterized by their heightened sensitivity within the visible spectrum and rapid response times, making them well-suited for capturing light in real-time scenarios [33].

In this study, a transparent and flexible 1T-1D image sensor array on a flexible CPI substrate is successfully implemented using laser lift-off (LLO) techniques. By utilizing transparent ITO electrodes and a-IGZO channel-based TFT backplanes, vertically aligned p-i-n a-Si:H photodiodes are monolithically integrated. These photodiodes are fabricated using a low-temperature (<90 °C) deposition process using the PECVD method and are densely packed in a 14 × 14-pixel configuration. Notably, the low-temperature-processed a-Si:H photodiodes exhibit photo-responsible performance metrics, demonstrating a responsivity (R) of 31.43 mA/W and a detectivity (D*) of 3.0×10^{10} Jones (biased at −1 V) at a wavelength of 470 nm. Furthermore, the flexible image sensor arrays exhibit exceptional mechanical durability. They can be attached to curved surfaces with bending radii from 5 to 20 mm, enduring up to 1000 cycles stably. These findings show considerable promise for the integration of flexible active-matrix technology, particularly for real-time optical signal detection in spatial applications.

2. Materials and Methods

Synthesis of CPI film and LLO process: The glass substrate was cleaned via sonication in acetone, isopropyl alcohol (IPA), and deionized water (D.I. water) for 5 min. After cleaning, the glass was dried in an oven at 100 °C for 5 min. Subsequently, the cleaned glass substrate was loaded into a plasma-enhanced chemical vapor deposition chamber (PECVD, SNTEK, Anseong, Republic of Korea), and an a-Si:H sacrificial layer with a thickness of approximately 100 nm was deposited after generating plasma with very high-frequency (VHF) 30 W power under H_2 and SiH_4 conditions at 250 °C and 400 mTorr. To form the CPI film, we prepared a solution by stirring IPI-C (5000 cps, solid content = 18.5 wt%, IPITECH, Daejeon, Republic of Korea) and 3-glycidoxypropyltrimethoxysilane (98%, Sigma-Aldrich, St. Louis, MO, USA) together. The solution was then spin-coated onto the a-Si:H-deposited glass substrate at a rotation speed of 400 rpm. The solution-coated glass substrate was annealed at 350 °C for 4 h in a box furnace (Thermal System and Technology, Hwaseong, Republic of Korea). The a-Si:H sacrificial layer sandwiched between the glass substrate and the CPI film was removed using a laser with a wavelength of 532 nm. The laser was controlled using an external attenuator, frequency, and diode current (Kortherm Science, Incheon, Republic of Korea).

Fabrication of a-IGZO TFT backplane: The surface roughness of the CPI film after the LLO process was reduced by depositing a 50 nm thick Al_2O_3 buffer layer using atomic layer deposition (ALD, Lucida M 100, NCD, Seoul, Republic of Korea) [34]. The deposition was carried out at 200 °C utilizing a trimethylaluminium ($(CH_3)_3Al$, TMA) precursor and H_2O [35]. The 80 nm thick ITO gate electrode was fabricated via direct current (DC) magnetron sputter at room temperature (R.T) with Ar flow at 25 sccm and O_2 flow at 0.18 sccm under 3.50 mTorr of pressure. After deposition, the ITO gate electrode was defined by a photolithography process followed by the selective wet etching of the ITO using copper etchant solution (Sigma-Aldrich, USA). Following that, a 50 nm Al_2O_3 gate dielectric layer was deposited using the ALD system with the TMA precursor and H_2O at 200 °C. For the 40 nm thick a-IGZO (In_2O_3:Ga_2O_3:ZnO = 1:1:2, TASCO, Anyang, Republic of Korea) channel, 3-inch radio frequency (RF) sputter (Ultech, Daegu, Republic of Korea) was employed at R.T. with Ar flow at 25 sccm and RF power set at 80 W under 8 mTorr of pressure. After deposition, a photolithography process was carried out for channel patterning, followed by the selective wet etching of a-IGZO using 1 M hydrochloric acid solution (HCl, Samchun Chemical Co., Seoul, Republic of Korea). Subsequently, S/D patterning was patterned the utilization of the photolithography process. Following this, ITO source and drain (S/D) electrode deposition was conducted using a DC magnetron sputtering technique at room temperature, maintaining a working pressure of 3.50 mTorr. The deposition process was carried out with a controlled Ar flow rate of 25 sccm and an O_2 flow rate of 0.18 sccm. The lift-off process used acetone sonication. Finally, a 50 nm thick Al_2O_3 passivation layer was deposited using the ALD system with the TMA precursor and H_2O at 200 °C.

Fabrication of p-i-n a-Si:H PD: First, to open the bottom ITO electrodes connected to the drain electrodes of the a-IGZO TFTs, photolithography patterning was employed. Subsequently, phosphoric acid (H_3PO_4 Samchun Chemical Co., Republic of Korea) etching was conducted at 55 °C for 40 s to etch away 50 nm of the Al_2O_3 passivation layer. Afterward, to prevent damage to the ITO electrodes from plasma exposure, a 30 nm thick layer of aluminum zinc oxide (AZO) was deposited using DC magnetron sputtering. Next, three layers of n-Si (20 nm), i-Si (400 nm), and p-Si (30 nm) were deposited using PECVD. Finally, the ITO top electrode was deposited to a thickness of 200 nm using DC magnetron sputtering at room temperature with Ar flow at 20 sccm and O_2 flow at 0.18 sccm under 3.50 mTorr of pressure.

Characterization: The elemental composition of a-IGZO was analyzed utilizing XPS (NEXSA, Thermo Fisher Scientific, Waltham, MA, USA). The cross-sectional and elemental analyses of both the a-IGZO TFT and the a-Si:H photodiode were conducted via SEM imaging and EDS mapping. The electrical performance assessment was carried out using the Keithley 4200-SCS semiconductor analyzer system at room temperature and under atmospheric pressure conditions. For light measurements, a controlled environment was maintained within a dark shield box (MSD1, MS tech), where an LED controller (BioLED light source control module, Mightex, Toronto, ON, Canada) and a 470 nm light source (BLS-LCS-0470-03-22, Mightex) were connected. Furthermore, the flexibility of the image sensor was evaluated by performing bending tests using a linear stage (M-433, Newport, Irvine, CA, USA).

3. Result and Discussion

3.1. Device Structure and Fabrication

Figure 1a illustrates the overall 3D scheme of an a-IGZO TFT and an a-Si:H photodiode (1T-1D) image sensor. The monolithic integrated image sensor consists of an a-IGZO thin-film transistor for sensing and switching and an a-Si:H p-i-n photodiode for photo conversion. In this device configuration, the role of the a-IGZO TFT is to regulate its on/off states through the gate field, effectively managing current flow because of its high conductivity and rapid response characteristics. Furthermore, the p-i-n a-Si:H photodiode transforms incoming light into electrical signals via the photoelectric effect. Incident

light generates charge carriers (electron–hole pairs) in the i-layer, converting light energy into electrical signals. Integrating a photodiode within the 1T-1D structure enables light-induced electron–hole pair generation. Figure 1b shows a scanning electron microscopy (SEM) image of the 1T-1D configuration. Also, an optical microscopy (OM) image of the monolithic integration of the image sensor array is depicted in Figure 1c. Figure 1d shows an atomic force microscope (AFM) image of the a-IGZO surface. An AFM analysis was conducted in a selected area of 1000 nm × 1000 nm, and the root mean square (RMS) roughness was approximately 0.06 nm. This result shows that the surface of the a-IGZO has excellent uniformity [36,37].

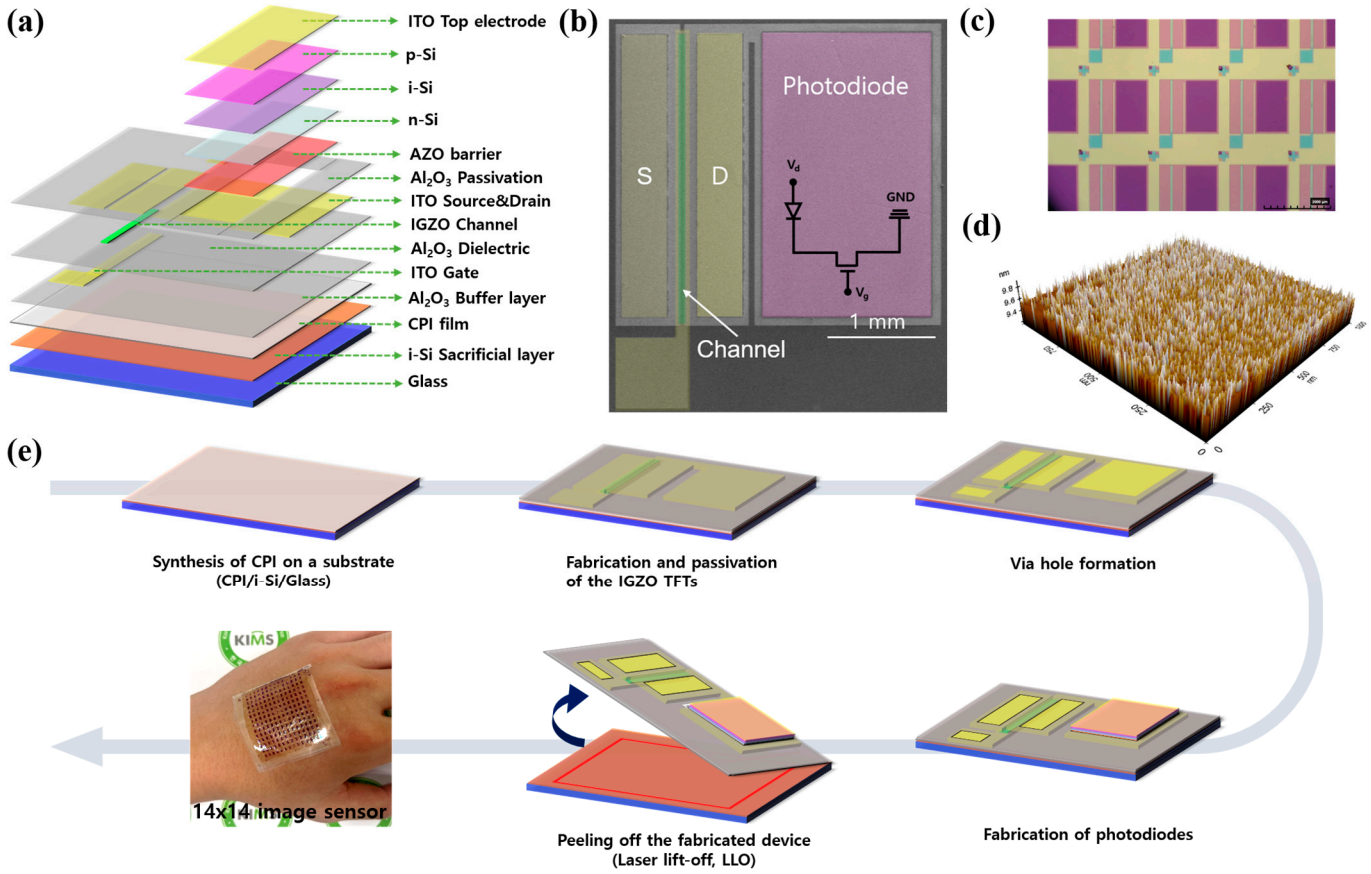


Figure 1. (**a**) Schematic of the a-IGZO TFT and a-Si:H photodiode. (**b**) SEM image of a-IGZO TFT/a-Si:H photodiode. (**c**) Optical microscopy (OM) image of the monolithic integration of the image sensor array. (**d**) AFM image of IGZO. (**e**) Schematic fabrication process of a-IGZO TFT/a-Si:H photodiode integration and image of a flexible 1T-1D structure image sensor on CPI film.

Figure 1e presents the overall fabrication process for the vertically stacked 1T-1D image sensor array. In order to fabricate the flexible 1T-1D image sensor array on a flexible substrate, LLO was used to release the device on the rigid glass substrate [34,38]. Initially, a CPI film was uniformly coated with a thickness of 20 um on a glass substrate with an area of 5 × 5 cm^2. Subsequently, a-IGZO TFTs with bottom local-gate structures were manufactured using the conventional photolithography technique. To maintain the optical transparency of our flexible TFTs, the ITO electrodes were used to form the gate, source, and drain electrodes. Then, a p-i-n a-Si:H was deposited using PECVD at a temperature of 90 °C. Finally, the CPI film was peeled off from the glass substrate using the LLO process. A comprehensive schematic of the intricate component fabrication process is illustrated in Figure S1. Furthermore, we present optical microscopy (OM) images captured of each fabrication step in Supplementary Figure S2. Additionally, the transmittance spectra of the IGZO film deposited on the glass substrate are shown in Figure S3.

SEM and energy-dispersive X-ray spectroscopy (EDS) maps are also shown to analyze the distribution of elements within the a-IGZO and a-Si:H photodiode, confirming the homogeneous distribution of the elements, as shown in Figure 2a,b. Additionally, a surface analysis of the a-IGZO channel material using X-ray photoelectron spectroscopy is shown in Figure S4. At the In 3d peak, the binding energy values for In $3d^{5/2}$ and In $3d^{3/2}$ were observed at 444.1 and 452 eV, respectively. These are attributable to the In^{3+} binding state in the IGZO. At the Ga 2p peak, the binding energy values for Ga $2p^{3/2}$ and Ga $2p^{1/2}$ were found to be 1117.3 and 1144.1 eV, respectively, indicating Ga^{3+} binding states in the IGZO. At the Zn 2p peak, the binding energy values for Zn $2p^{3/2}$ and Zn $2p^{1/2}$ were determined as 1021.3 and 1044.4 eV, respectively, suggesting Zn^{2+} binding states in the IGZO. The O 1s peak of the IGZO separates into two peaks at 529.8 and 531 eV. The lower binding energy peak (529.8 eV) corresponds to the binding energy of the lattice oxygen (metal-oxide, O_I), while the peak at 531 eV is associated with non-lattice oxygen (oxygen vacancy, O_{II}). The areas obtained from the deconvolution of the O 1s peak (A_{OI} and A_{OII}) are utilized for the quantitative analysis of oxygen vacancies in the IGZO film using the following formulae [39,40]:

$$O_I\ (\%) = \frac{AOI}{AOI + OII} \times 100 \quad (1)$$

$$O_I\ (\%) = \frac{AOII}{AOI + OII} \times 100 \quad (2)$$

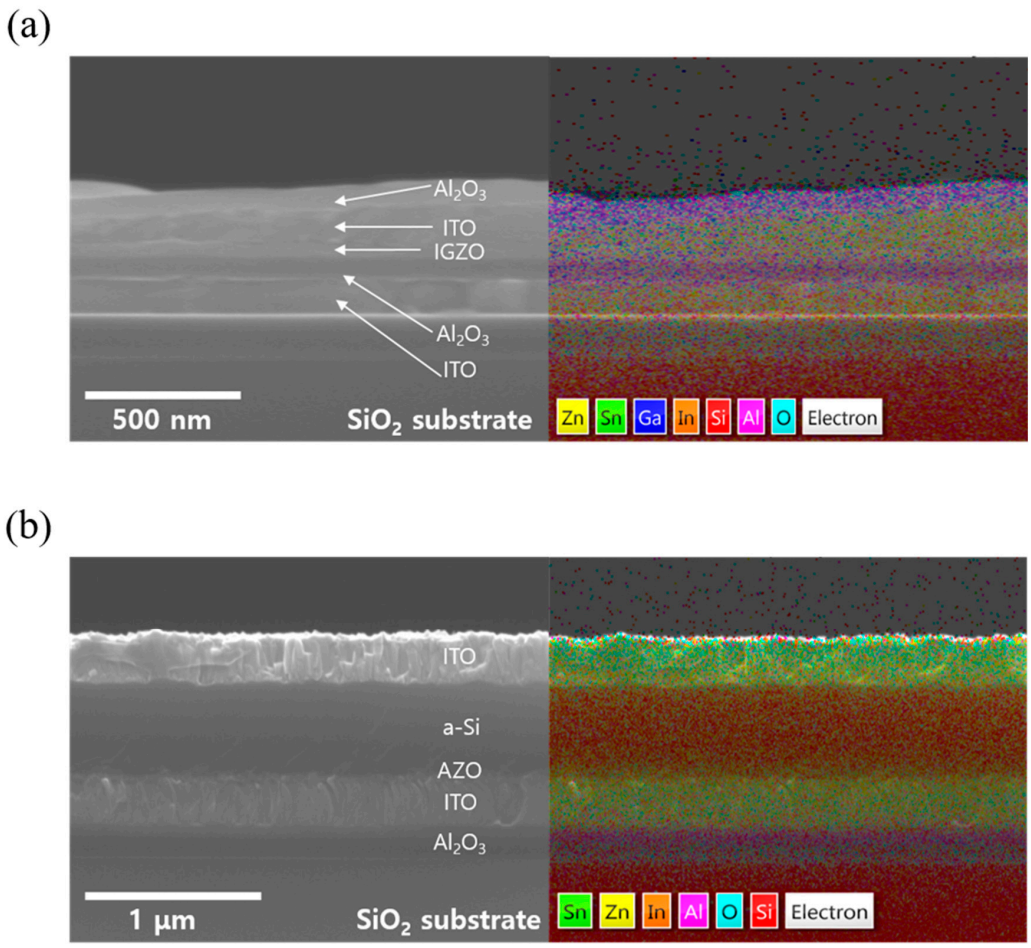


Figure 2. (**a**) SEM cross-section image and EDS map of the a-IGZO TFT. (**b**) SEM cross-section image and EDS map of the p-i-n a-Si:H photodiode.

Equations (1) and (2) are used to calculate the O_I and O_{II} area ratios of IGZO. The extracted IGZO O_I and O_{II} area ratios are 60.90% and 39.10%, respectively.

3.2. Electrical Characteristics of a-IGZO TFT Backplanes

The vertical scheme and electrical measurement configuration for the 1T-1D device cell are shown in Figure 3a. Figure 3b shows the transfer characteristics (I_d-V_g) measured with 196 individual a-IGZO TFTs. The overall 196 a-IGZO TFTs fabricated on CPI flexible film show a device yield of 100 %, and the device could work well with tight distribution and low variability. This means that uniform switching functionality connected to a-Si photodiodes is possible. The output characteristics (I_d-V_d) were investigated while varying the gate voltage (V_g) from 0 to 15 V in increments of 1 V, as shown in Figure 3c. This investigation revealed a consistent increase in drain current (I_d) as V_g increased.

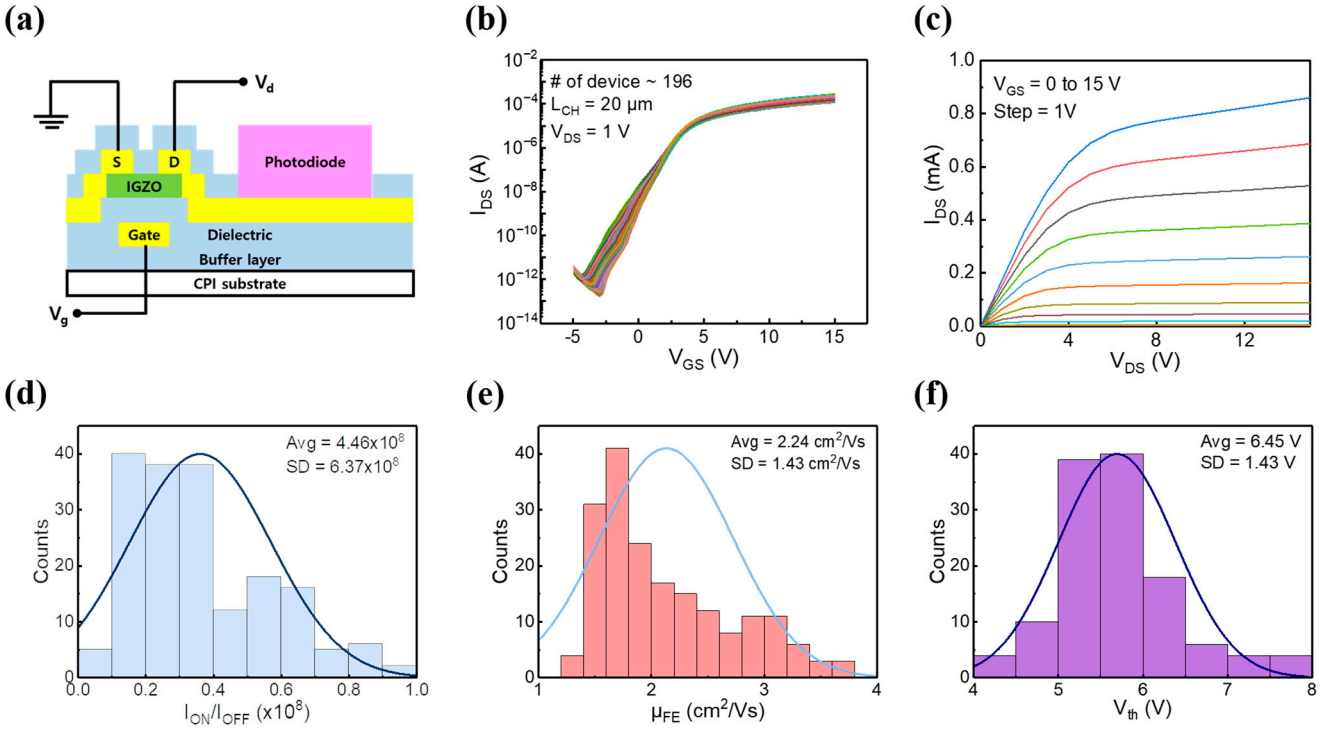


Figure 3. (**a**) Illustration of the transistor measurement method. (**b**) Transfer characteristics after 1T-1D integration when V_d is 1 V. (**c**) Output characteristic after integration when V_{GS} is 0–15 V. (**d**) On/off ratios, (**e**) field-effect mobilities, (**f**) and threshold voltages calculated for the characteristics of the 1T-1D integrated transistor.

Figure 3d,e present statistical histograms depicting the device parameters for the on/off ratio and field-effect mobility, respectively. The average value of the on/off ratio (I_{on}/I_{off}) was found to be about 10^8. The field-effect mobility (μ_{FE}) was determined with an average value of 2.24 $cm^2/V{\cdot}s$ and a standard deviation of 1.43, calculated using the following formula:

$$\mu_{FE} = \left(\frac{dI_D}{dV_G}\right)\left(\frac{L}{V_D C_{ox} W}\right) \quad (3)$$

In this equation, I_D, V_G, L, V_D, C_{ox}, and W represent the source-drain current, the gate voltage, the channel length, the drain voltage, the gate capacitance of the Al_2O_3 dielectrics, and the channel width, respectively.

Figure 3f illustrates the statistical distribution of threshold voltage (V_{th}) for a total of 196 individual a-IGZO TFTs. The average value and standard deviation are estimated to be approximately 6.45 and 1.43 V, respectively. As a result, the fabricated a-IGZO TFT array shows good uniformity and reproducibility. A comparison of the electrical characteristics between the a-IGZO-isolated TFTs and those of the TFT after photodiode integration

is depicted in Figure S5. It is confirmed that there is a negligible change in the device parameters for the on/off ratio and the field-effect mobility.

3.3. Photoresponsivity Characteristics

The images of the measurements in dark and photo conditions are presented in Figure S6. Dark current measurements were performed in a dark shield box to block all external light. For photocurrent measurements, the device was positioned at a 5 cm distance from the light source within the dark shield box, and the light intensity was controlled under a wavelength of 470 nm light illumination.

Figure 4a,b illustrate the J-V characteristics of a p-i-n a-Si:H photodiode and the transfer characteristics upon the integration of an a-IGZO TFT with a p-i-n a-Si:H photodiode. It was found that the photocurrent also increased as the light intensity increased. Figure 4c shows the photocurrent behavior as an increase in light intensity, directly correlating with a proportional rise in photocurrent. The p-i-n a-Si:H photodiode operates on the principle of generating electron–hole pairs upon light illumination. Increasing light intensity induces a proportional increase in the creation of electron–hole pairs. Subsequently, these generated electron–hole pairs facilitate the generation of electric current as they traverse the material, thereby leading to an augmented photocurrent output. The photocurrent exhibited an almost linear correlation with the increasing voltage, suggesting the formation of ohmic contact between the top and bottom and top ITO electrodes within the a-Si:H photodiode structure. At a voltage bias of 1 V, the photocurrent (I_{ph}), characterized as a function of incident light intensity, was evaluated utilizing a simplified power law equation, as depicted in Figure 4c. In this equation, A signifies the wavelength constant of the incoming light. Additionally, the power law equation is calculated using the following formula:

$$I_{ph} = A \times P^{\alpha} \quad (4)$$

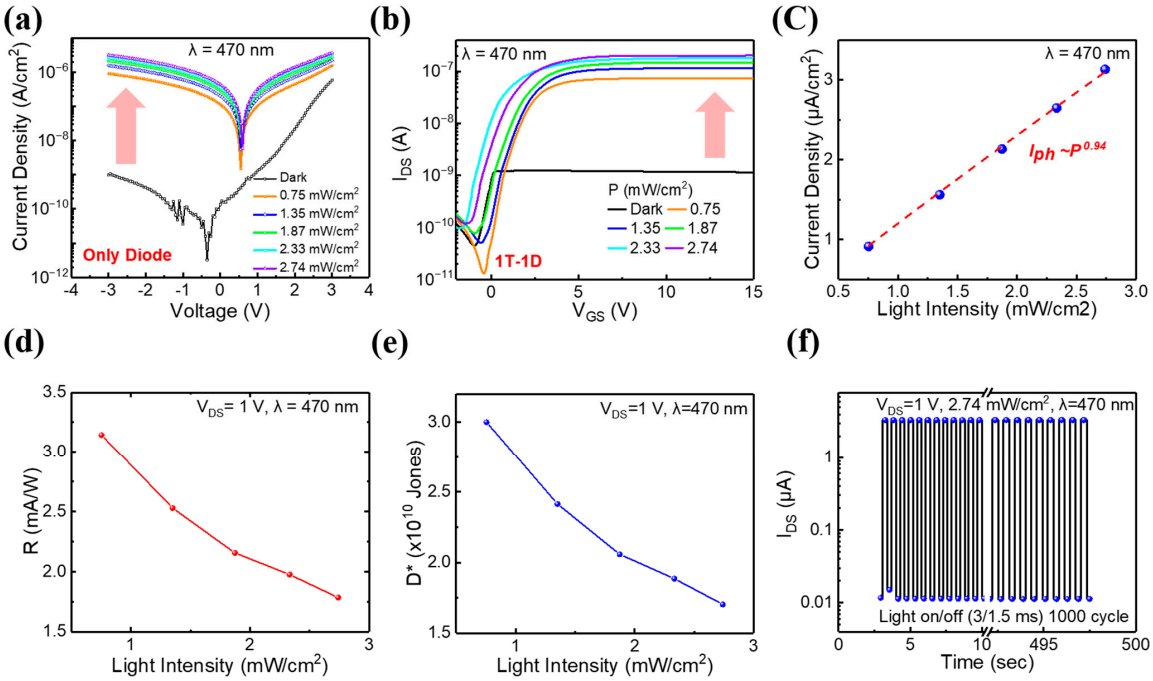


Figure 4. (**a**) J-V curve of the p-i-n a-Si:H photodiode under dark and light illumination at V_{DS}—3 V (470 nm). (**b**) Transfer characteristics of a 1T-1D pixel exposed to various light intensities when V_{DS} is 1 V. (**c**) Photocurrent of p-i-n a-Si:H photodiode at various light intensities (470 nm). (**d**) Responsivity of p-i-n a-Si:H photodiode at various light intensities (470 nm). (**e**) Detectivity of p-i-n a-Si:H photodiode at various light intensities (470 nm). (**f**) Photoresponse under pulsed light illumination at 3 ms with 1000 cycles.

In the power law equation, P represents the applied light intensity, and α corresponds to the exponent denoting the degree of photosensitivity [41]. The experimental data exhibited a favorable fit with the power law equation, exhibiting a linearity of 0.94 [42]. Figure 4d,e illustrate that the important parameters in the evaluation of photodiode effectiveness are the dependence of responsivity (R) and specific detectivity (D*) on incident light intensity. These two parameters can be obtained from the following formulas:

$$\mathrm{R} = \frac{I_{ph}}{P_{opt} \cdot A} \tag{5}$$

$$\mathrm{D}^* = \mathrm{R}\sqrt{\frac{AB}{\overline{i_n^2}}} \tag{6}$$

In this equation, I_{ph}, P_{opt}, A, B, and $\overline{i_n^2}$ are the photocurrent, light intensity, effective area, frequency bandwidth, and mean-square noise current measured at a bandwidth of 100 Hz in darkness, respectively [43]. Figure 4d,e illustrate the R and D* responses at −1 V for various light intensities. The maximum responsivity of 31.43 mA/W was accompanied by a specific detectivity value of 3.00×10^{10} Jones (1 Jones = 1 cm $\mathrm{Hz}^{1/2}$/W). Responsivity quantifies the efficiency of light-to-electrical-signal conversion, whereas detectivity evaluates the device's ability to discern weak signals despite background noise. The measurement plots of the noise current within a frequency range of 1 Hz to 10 kHz in an integrated image sensor containing a-IGZO TFT and a-Si:H photodiodes are presented in Figure S7.

The dynamic photoresponse of the p-i-n a-Si:H photodiode was observed as depicted in Figure 4f. This response was observed under a cycle of on/off lasers (470 nm) at intervals of 0.3 s, repeating in cycles of 1000. The drain current increased during illumination and decreased upon the deactivation of the laser. The rise time (τ_r) associated with on/off light is approximately 140 ms, while the fall time (τ_f) is 21 ms, as shown in Figure S8. This photodynamic response persists for 500 s over 1000 on/off cycles, showcasing repetitive and stable light reactions [44].

Figure 5 shows the photocurrent mapping using an active pixel image sensor of a 14×14 array, showing "K", "I", "M", and "S". The number of devices corresponding to each character is 76 for K and I, 116 for M, and 98 for S. Except for the parts corresponding to the characters in the four characters, the shadow mask was covered and measured at V_{DS} = 1 V and V_{GS} = 15 V. The part receiving external light illumination is expressed as I_{ph}. Accordingly, these results show the excellent operational performance of an integrated image sensor that combines a-IGZO TFT and p-i-n a-Si:H photodiodes, demonstrating remarkable electrical and optical uniformity [45].

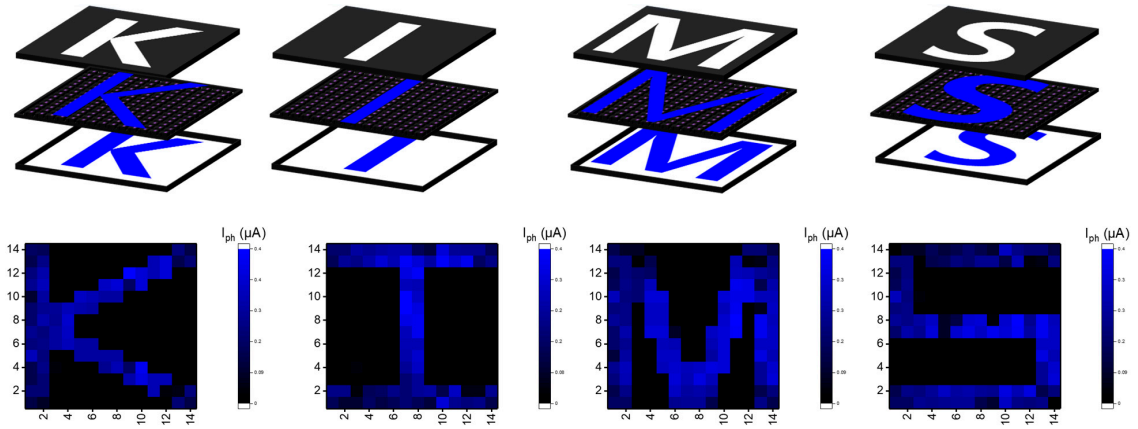


Figure 5. Schematic representation showing patterned I_{ph} mapping on a 14×14 active pixel image sensor array in a 1T-1D configuration under 2.74 mW/cm^2 at a wavelength of 470 nm.

3.4. Structural Flexibility

Flexibility and rollability are crucial mechanical attributes that play a significant role in the operation of flexible image sensors [42]. An integrated image sensor has been developed, featuring a combination of a-IGZO TFTs and a-Si:H photodiodes fabricated on a flexible CPI film. Remarkably, this integrated sensor maintains its performance integrity even when subjected to rigorous bending tests and high bending radii, as detailed in Table 1. Figure 6a presents images from a 1T-1D image sensor in a bending state with a diameter of 20 mm. Photoelectric measurements were conducted for various diameters, ranging from 10 to 40 mm. Figure 6b depicts the photo and dark states measured based on the transfer characteristics (V_d = 1 V, V_g = 15 V) with various bending radii: flat, 5, 10, 15, and 20 mm. Few differences in the dark current and photocurrent were found when the bending radii (r) varied at 5 mm, 10 mm, 15 mm, and 20 mm. Figure 6c demonstrates the dynamic response when applying a light pulse with a 0.3 s duration for approximately 600 s at V_d = 1 V while the bending radius was set at 5 mm. The rise time is approximately 200 ms, and the fall time is around 300 ms. The photodynamic response exhibits a repeated stable photoresponse for 600 s, indicating that few current variations could be observed.

Table 1. Comparison of recently reported a-IGZO transistor/photodiode image sensors.

Device	Processing Temperature (°C)	Responsivity (mA/W)	Number of Array (EA)	Flexibility (Bending Radius/Bending Cycle)	Measurement Conditions	Reference
IGZO/a-Si:H	<90	31.43	14 × 14	>5 mm/>1000 cycle	λ = 470 nm	This work
IGZO/Perovskite/P3HT	<180	400	12 × 12	-	λ = 850 nm	[17]
IGZO/Perovskite/PCBM/BCP	-	340	12 × 12	-	λ = 550 nm	[18]
IGZO/Perovskite	-	200	12 × 12	-	λ = 530 nm	[43]

In Figure 6d, images from a flexible image sensor integrated with a 1T-1D structure under upward bending are shown. Maximum upward bending is applied with a bending radius of 5 mm in 200 bending cycles, ranging from 200 to 1000 cycles. Figure 6e illustrates the corresponding photo and dark states measured based on the transfer characteristics (V_d = 1 V, V_g = 15 V) with respect to the bending cycles. This reveals that the difference in current between the dark and photocurrent states remains low despite the bending cycles. Figure 6f displays light pulse measurements of the image sensor taken during a 1000-cycle upward bending test, where V_d is set at 1 V for approximately 600 s. Similar to previous observations, τ_r is about 200 ms, τ_f is around 300 ms, and there is little current difference.

In Figure 6g, images acquired from the flexible image sensor integrated with a 1T-1D structure under downward bending are displayed. Similar to the upward bending test, measurements were conducted with maximum incremental downward bending with a bending radius of 5 mm over 200 bending cycles, ranging from 200 to 1000 cycles. Figure 6h depicts the corresponding and transfer characteristics (V_d = 1 V, V_g = 15 V) based on the bending cycles. The difference in current change between the dark and photo states remains negligible. Furthermore, Figure 6i showcases light pulse measurements of the image sensor during a 1000-cycle downward bending test, with V_d set at 1 V for approximately 600 s. These results show its remarkable mechanical and physical durability.

Additionally, the deformation ratio exerted on each device according to its diameter was calculated, as described below:

$$\varepsilon_{TFT}\ (\%) = (t_{CPI} + t_{Al_2O_3} + t_{ITO} + t_{a-IGZO})\ /\varnothing \times 100 \quad (7)$$

$$\varepsilon_{Photodiode}\ (\%) = (t_{CPI} + t_{Al2O3} + t_{ITO} + t_{a-Si:H})\ /\varnothing \times 100 \quad (8)$$

In this equation, ε, t, and $\varnothing$, are the strain, thickness of the layer, and diameter of the device [34]. The stable and reproducible endurance characteristics remain even after undergoing 1000 cycles, even when the device is folded to a diameter of 5 mm (ε_{tft} = 0.20%/$\varepsilon_{photodiode}$ = 0.21%). A comparison of the dark current and photocurrent, as

indicated by the J-V characteristics measured under different bending radii and bending cycles, is illustrated in Figures S9 and S10.

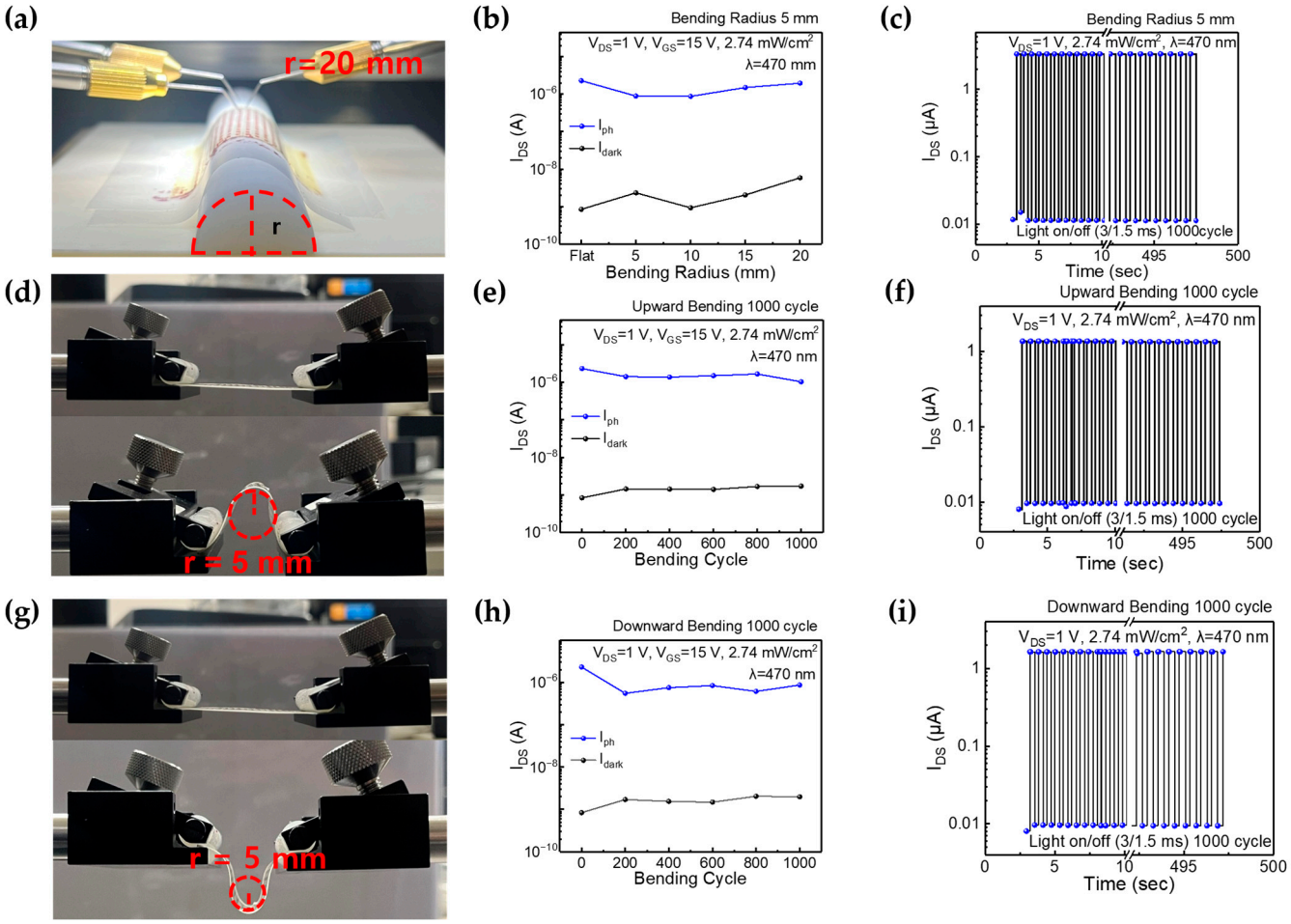


Figure 6. (**a**) When a bending radius of 20 mm was applied and measured, an image was obtained. (**b**) The difference in current between the dark and photo states of the 1T-1D integration transfer curve, with a bending radius of 5 mm applied (Vd = 1 V, Vg = 15 V). (**c**) Photoresponse under pulsed light illumination at 3 ms with 1000 cycles for a bending radius of 5 mm. (**d**) The image in the flat-upward bending radius in a 5 mm state. (**e**) The difference in current between the dark and photo states of the 1T-1D integration transfer curve after performing 1000 cycles of flat-upward bending with a radius of 5 mm. (**f**) Photoresponse under pulsed light illumination at 3 ms with 1000 cycles for a flat-upward bending radius of 5 mm after 1000 cycles. (**g**) The image is in a flat-downward bending radius 5 mm state. (**h**) The difference in current between the dark and photo states of the 1T-1D integration transfer curve after performing 1000 cycles of flat-downward bending with a radius of 5 mm. (**i**) Photoresponse under pulsed light illumination at 3 ms with 1000 cycles for a flat-downward bending radius of 5 mm after 1000 cycles.

4. Conclusions

In this study, we successfully synthesized p-i-n a-Si:H photodiodes at low process temperatures (<90 °C) and integrated them with a-IGZO TFTs to achieve a transparent 1T-1D-structured image sensor array. The implementation of this structure on a flexible ultrathin CPI film substrate exhibited remarkable on/off ratios and field-effect mobility. Furthermore, under a 470 nm wavelength, the image sensor demonstrated excellent responsivity exceeding 31.43 mA/W, along with exceptional uniformity and yield. Remarkably, even after undergoing more than 500 bending tests, the device maintained superior flexibility and mechanical stability.

In conclusion, our research establishes the feasibility of a transparent 1T-1D image sensor array composed of p-i-n a-Si:H photodiodes and a-IGZO TFTs, synthesized at low process temperatures. The exceptional performance, including impressive responsivity, uniformity, and mechanical stability, positions this integrated structure as a promising candidate for a wide range of flexible and transparent electronic applications. Our findings underscore the potential of this technology to drive advancements in the field of flexible electronics and pave the way for innovative applications in various industries.

Supplementary Materials: The following supporting information can be downloaded at: https://www.mdpi.com/article/10.3390/nano13212886/s1, Figure S1. Detailed schematic fabrication process for a 1T-1D integrated image sensor of flexible a-IGZO TFT/a-Si:H photodiode on CPI film. Figure S2. OM image illustrating the fabrication process of a 1T-1D structured image sensor. Figure S3. Transmittance spectra of the a-IGZO thin film on the glass substrate. Figure S4. XPS spectra of the a-IGZO (a) In 3d (b) Ga 2p (c) Zn 2p (d) O 1s. Figure S5. Comparison of Transfer Characteristics before and after Integration of a-Si:H Photodiode with a-IGZO TFT. Figure S6. (a) Image of during the measurement of Dark current within the Dark box (b) Image of while measuring Photo current. Figure S7. The noise current measurements of an integrated image sensor with a-IGZO tft and a-Si:H photodiodes in across a frequency range from 1 Hz to 10 kHz. Figure S8. The rise time (140 ms) and fall time (21 ms) exhibited during the modulation of the light pulse on/off. Figure S9. The variation in current with respect to bending radius when subjected to a light intensity of 2.74 mW/cm^2 at a wavelength of 470 nm. Figure S10. The current variation of J-V characteristics in response to bending cycles when exposed to upward bending and downward bending conditions under a light intensity of 2.74 mW/cm^2 at a wavelength of 470 nm.

Author Contributions: D.C. and J.-W.S. designed and conducted the experiments. J.Y. supported the execution of the experiments and the data analysis. S.M.Y. supported the analysis of the SEM experiment. Y.K., J.Y. and D.C. wrote the paper. S.-K.L., J.-D.K. and Y.K. supported and guided the experiments and the analysis of the results. Y.K. conceived the project and supervised the writing of the paper. All authors have read and agreed to the published version of the manuscript.

Funding: This study was supported by the Fundamental Research Program (PNK9020) of the Korean Institute of Materials Science (KIMS) and the Technology Innovation Program (20022508, Development of Ultrahigh Temperature Activator and Core Process Technology for SiC Devices) of the Ministry of Trade, Industry, and Energy (MOTIE, Korea). This work was also supported by a National Research Foundation of Korea (NRF) grant funded by the Korean government (MSIT; Ministry of Science and Information Technology) (No. 2020M3H4A308182013). This study was supported by the Energy Technology Development Program of the Korean Institute of Energy Technology Evaluation and Planning (KETEP) (Grant No. RS-2023-00301944).

Data Availability Statement: The data that support the findings of this study are available from the corresponding author upon reasonable request.

Conflicts of Interest: The authors declare no conflict of interest.

References

1. Yoon, J.; Bae, G.-Y.; Yoo, S.; Yoo, J.I.; You, N.-H.; Hong, W.-K.; Ko, H.C. Deep-ultraviolet sensing characteristics of transparent and flexible IGZO thin film transistors. *J. Alloys Compd.* **2020**, *817*, 152788. [CrossRef]
2. Zhang, L.; Wei, J.; Zhou, K.; Wan, C.; Sun, H. Highly transparent IGZO-TFTs uses IGZO source and drain electrodes with a composite insulation layer structure. *Optik* **2020**, *204*, 163654. [CrossRef]
3. Munzenrieder, N.; Cherenack, K.H.; Troster, G. The Effects of Mechanical Bending and Illumination on the Performance of Flexible IGZO TFTs. *IEEE Trans. Electron Devices* **2011**, *58*, 2041–2048. [CrossRef]
4. Chien, C.-W.; Wu, C.-H.; Tsai, Y.-T.; Kung, Y.-C.; Lin, C.-Y.; Hsu, P.-C.; Hsieh, H.-H.; Wu, C.-C.; Yeh, Y.-H.; Leu, C.-M.; et al. High-Performance Flexible a-IGZO TFTs Adopting Stacked Electrodes and Transparent Polyimide-Based Nanocomposite Substrates. *IEEE Trans. Electron Devices* **2011**, *58*, 1440–1446. [CrossRef]
5. Kim, Y.-S.; Oh, H.-J.; Shin, S.; Oh, N.; Park, J.-S. Enhanced performance and stability in InGaZnO NIR phototransistors with alumina-infilled quantum dot solid. *Sci. Rep.* **2022**, *12*, 12167. [CrossRef]
6. Shiah, Y.-S.; Sim, K.; Shi, Y.; Abe, K.; Ueda, S.; Sasase, M.; Kim, J.; Hosono, H. Mobility–stability trade-off in oxide thin-film transistors. *Nat. Electron.* **2021**, *4*, 800–807. [CrossRef]

7. Dhara, S.; Niang, K.M.; Flewitt, A.J.; Nathan, A.; Lynch, S.A. Tail state mediated conduction in zinc tin oxide thinfilm phototransistors under below bandgap optical excitation. *Sci. Rep.* **2021**, *11*, 19016. [CrossRef]
8. Sheng, J.; Hong, T.; Lee, H.M.; Kim, K.; Sasase, M.; Kim, J.; Hosono, H.; Park, J.S. Amorphous IGZO TFT with High Mobility of approximately 70 cm^2/(V s) via Vertical Dimension Control Using PEALD. *ACS Appl. Mater. Interfaces* **2019**, *11*, 40300–40309. [CrossRef]
9. Jae Kwang, U.; Suhui, L.; Seonghyun, J.; Mativenga, M.; Se Yun, O.; Choong Hun, L.; Jin, J. High-Performance Homojunction a-IGZO TFTs With Selectively Defined Low-Resistive a-IGZO Source/Drain Electrodes. *IEEE Trans. Electron Devices* **2015**, *62*, 2212–2218. [CrossRef]
10. Sun, Y.; Fan, J.; Liu, M.; Zhang, L.; Jiang, B.; Zhang, M.; Zhang, X. Highly transparent, ultra-thin flexible, full-color mini-LED display with indium–gallium–zinc oxide thin-film transistor substrate. *J. Soc. Inf. Display* **2020**, *28*, 926–935. [CrossRef]
11. Kang, S.H.; Kang, S.; Park, S.C.; Park, J.B.; Jung, Y.; Hong, B.H. Silicon germanium photo-blocking layers for a-IGZO based industrial display. *Sci. Rep.* **2018**, *8*, 17533. [CrossRef]
12. Chen, Y.F.; Geng, D.; Jang, J. Integrated Active-Matrix Capacitive Sensor Using a-IGZO TFTs for AMOLED. *IEEE J. Electron Devices Soc.* **2018**, *6*, 214–218. [CrossRef]
13. Hara, Y.; Kikuchi, T.; Kitagawa, H.; Morinaga, J.; Ohgami, H.; Imai, H.; Daitoh, T.; Matsuo, T. IGZO-TFT technology for large-screen 8K display. *J. Soc. Inf. Display* **2018**, *26*, 169–177. [CrossRef]
14. Wang, Y.; Liao, C.; Zhang, S. P-8: A Depletion-Mode Compatible Gate Driver on Array for a-IGZO TFT-OLED Displays. In *SID Symposium Digest of Technical Papers*; Wiley Online Library: Hoboken, NJ, USA, 2019; pp. 1241–1244.
15. Jack Fan, C.-Y.L.; Chen, S.-J.; Jun, Z.L.; Yang, S.; Cai, L.M.; Fei, X.H.; Nian, L. High transparent Active matrix Mini-LED Full Color Display with IGZO TFT Backplane. *SID Symp. Dig. Technol. Pap.* **2019**, *50*, 454–456.
16. Hu, Y.B.; Guo, L.Q.; Huo, C.H.; Dai, M.Z.; Webster, T.J.; Ding, J.N. Transparent Nano Thin-Film Transistors for Medical Sensors, OLED and Display Applications. *Int. J. Nanomed.* **2020**, *15*, 3597–3603. [CrossRef]
17. Wang, Y.; Chen, C.D.; Zou, T.Y.; Yan, L.Z.; Liu, C.; Du, X.Z.; Zhang, S.D.; Zhou, H. Spin-On-Patterning of Sn-Pb Perovskite Photodiodes on IGZO Transistor Arrays for Fast Active-Matrix Near-Infrared Imaging. *Adv. Mater. Technol.-Us* **2020**, *5*, 1900752. [CrossRef]
18. Zou, T.Y.; Xiang, B.; Xu, Y.B.; Wang, Y.; Liu, C.; Chen, J.; Wang, K.; Dai, Q.; Zhang, S.D.; Noh, Y.Y.; et al. Pixellated Perovskite Photodiode on IGZO Thin Film Transistor Backplane for Low Dose Indirect X-Ray Detection. *IEEE J. Electron Devices Soc.* **2021**, *9*, 96–101. [CrossRef]
19. Chen, T.; Wang, C.Y.; Yang, G.S.; Lou, Q.; Lin, Q.P.; Zhang, S.D.; Zhou, H. Monolithic Integration of Perovskite Photoabsorbers with IGZO Thin-Film Transistor Backplane for Phototransistor-Based Image Sensor. *Adv. Mater. Technol.-Us* **2023**, *8*, 2200679. [CrossRef]
20. Lee, J.; Georgitzikis, E.; Hermans, Y.; Papadopoulos, N.; Chandrasekaran, N.; Jin, M.; Siddik, A.B.; De Roose, F.; Uytterhoeven, G.; Kim, J.H. Thin-film image sensors with a pinned photodiode structure. *Nat. Electron.* **2023**, *6*, 590–598. [CrossRef]
21. Huang, W.-C.; Tseng, Z.-C.; Hsueh, W.-J.; Liao, S.-Y.; Huang, C.-Y. X-Ray Detectors Based on Amorphous InGaZnO Thin Films. *IEEE Trans. Electron Devices* **2023**, *70*, 3690–3694. [CrossRef]
22. Kamiya, T.; Hosono, H. Material characteristics and applications of transparent amorphous oxide semiconductors. *NPG Asia Mater.* **2010**, *2*, 15–22. [CrossRef]
23. Park, J.H.; Seok, H.J.; Jung, S.H.; Cho, H.K.; Kim, H.K. Rapid thermal annealing effect of transparent ITO source and drain electrode for transparent thin film transistors. *Ceram. Int.* **2021**, *47*, 3149–3158. [CrossRef]
24. Wang, B.; Thukral, A.; Xie, Z.; Liu, L.; Zhang, X.; Huang, W.; Yu, X.; Yu, C.; Marks, T.J.; Facchetti, A. Flexible and stretchable metal oxide nanofiber networks for multimodal and monolithically integrated wearable electronics. *Nat. Commun.* **2020**, *11*, 2405. [CrossRef] [PubMed]
25. Zhu, H.; Shin, E.S.; Liu, A.; Ji, D.; Xu, Y.; Noh, Y.Y. Printable Semiconductors for Backplane TFTs of Flexible OLED Displays. *Adv. Funct. Mater.* **2019**, *30*, 1904588. [CrossRef]
26. Wu, K.J.; Zhang, J.; Li, Y.B.; Wang, X.Z.; Liu, Y.; Yu, Q.; Chen, T.P. Design of AM Self-Capacitive Transparent Touch Panel Based on a-IGZO Thin-Film Transistors. *IEEE Access* **2020**, *8*, 76929–76934. [CrossRef]
27. Jang, Y.; Park, J.; Kang, J.M.; Lee, S.Y. Amorphous InGaZnO (a-IGZO) Synaptic Transistor for Neuromorphic Computing. *ACS Appl. Electron. Mater.* **2022**, *4*, 1427–1448. [CrossRef]
28. Lu, J.-H.; Jiang, B.-H.; Hsiao, F.-C.; Peng, Y.-C.; Su, Y.-W.; Lin, Y.-R.; Tsai, T.-H.; Shiu, M.-N.; Lin, C.-Y.; Fang, Y.-T. High-Performance organic photodiodes for Blue-Light hazard detection. *Chem. Eng. J.* **2022**, *437*, 135327. [CrossRef]
29. Yokota, T.; Fukuda, K.; Someya, T. Recent progress of flexible image sensors for biomedical applications. *Adv. Mater.* **2021**, *33*, 2004416. [CrossRef]
30. Feng, J.; Wang, Y.; Qin, X.; Lv, Y.; Huang, Y.; Yang, Q.; Li, G.; Kong, M. Revealing molecular mechanisms of colorless transparent polyimide films under photo-oxidation. *Polym. Degrad. Stab.* **2023**, *210*, 110294. [CrossRef]
31. Jang, H.-W.; Kim, K.-H.; Oh, S.; Yoon, S.-M. Analysis on Mechanical-Strain Induced Bias-Stress Instabilities for the Flexible InGaZnO Thin Film Transistors with Different Channel Geometries. In Proceedings of the 2019 26th International Workshop on Active-Matrix Flatpanel Displays and Devices (AM-FPD), Kyoto, Japan, 2–5 July 2019; IEEE: Piscataway, NJ, USA; pp. 1–4.

32. Djeffal, F.; Boubiche, N.; Ferhati, H.; Faerber, J.; Le Normand, F.; Javahiraly, N.; Fix, T. Highly efficient and low-cost multispectral photodetector based on RF sputtered a-Si/Ti multilayer structure for Si-photonics applications. *J. Alloys Compd.* **2021**, *876*, 160176. [CrossRef]
33. Bablich, A.; Müller, M.; Bornemann, R.; Nachtigal, A.; Haring Bolívar, P. High Responsivity and Ultra-Low Detection Limits in Nonlinear a-Si:H p-i-n Photodiodes Enabled by Photogating. *Photonic Sens.* **2023**, *13*, 230415. [CrossRef]
34. Hwang, Y.; Park, B.; Hwang, S.; Choi, S.W.; Kim, H.S.; Kim, A.R.; Choi, J.W.; Yoon, J.; Kwon, J.D.; Kim, Y. A Bioinspired Ultra Flexible Artificial van der Waals 2D-MoS_2 Channel/$LiSiO_x$ Solid Electrolyte Synapse Arrays via Laser-Lift Off Process for Wearable Adaptive Neuromorphic Computing. *Small Methods* **2023**, *7*, e2201719. [CrossRef]
35. Myers, T.J.; Throckmorton, J.A.; Borrelli, R.A.; O'Sullivan, M.; Hatwar, T.; George, S.M. Smoothing surface roughness using Al2O3 atomic layer deposition. *Appl. Surf. Sci.* **2021**, *569*, 150878. [CrossRef]
36. Ling, L.; Tao, X.; Zhongxiao, S.; Chunliang, L.; Fei, M. Effect of sputtering pressure on surface roughness, oxygen vacancy and electrical properties of a-IGZO thin films. *Rare Met. Mater. Eng.* **2016**, *45*, 1992–1996. [CrossRef]
37. Duan, M.; Zhang, S.; Ren, C.; Zhang, L.; Shao, Y. Impact of sputtering power of source/drain metal on performances of a-IGZO thin film transistors fabricated using wet back-channel-etch process. In Proceedings of the 2017 International Conference on Electron Devices and Solid-State Circuits (EDSSC), Hsinchu, Taiwan, 18–20 October 2017; IEEE: Piscataway, NJ, USA; pp. 1–2.
38. Choi, S.-W.; Park, J.-H.; Seo, J.-W.; Mun, C.; Kim, Y.; Song, P.; Shin, M.; Kwon, J.-D. Flexible and transparent thin-film light-scattering photovoltaics about fabrication and optimization for bifacial operation. *Npj Flex. Electron.* **2023**, *7*, 17. [CrossRef]
39. Yang, T.-T.; Kuo, D.-H.; Tang, K.-P. n-type Sn substitution in amorphous IGZO film by sol-gel method: A promoter of hall mobility up to 65 $cm^2/V{\cdot}s$. *J. Non-Cryst. Solids* **2021**, *553*, 120503. [CrossRef]
40. Kumar, A.; Krishnaiah, M.; Mishra, D.; Jo, H.; Jin, S.H. Role of IGZO thickness for oxygen reservoir control in stacked IGZO/ZrOx layers: Towards reliable, uniform performance of flexible random-access memories. *J. Alloys Compd.* **2022**, *922*, 166199. [CrossRef]
41. Wu, D.; Wang, Y.; Zeng, L.; Jia, C.; Wu, E.; Xu, T.; Shi, Z.; Tian, Y.; Li, X.; Tsang, Y.H. Design of 2D layered PtSe2 heterojunction for the high-performance, room-temperature, broadband, infrared photodetector. *ACS Photonics* **2018**, *5*, 3820–3827. [CrossRef]
42. Choi, J.M.; Jang, H.Y.; Kim, A.R.; Kwon, J.D.; Cho, B.; Park, M.H.; Kim, Y. Ultra-flexible and rollable 2D-MoS2/Si heterojunction-based near-infrared photodetector via direct synthesis. *Nanoscale* **2021**, *13*, 672–680. [CrossRef] [PubMed]
43. Zou, T.; Chen, C.; Xiang, B.; Wang, Y.; Liu, C.; Zhang, S.; Zhou, H. Flexible, active-matrix flat-panel image sensor for low dose X-ray detection enabled by integration of perovskite photodiode and oxide thin film transistor. In Proceedings of the IEEE International Electron Devices Meeting (IEDM), San Francisco, CA, USA, 7–11 December 2019.
44. Chanu, L.T.; Singh, N.K. Fast response photodetector analysis based on NiO nanowire using a catalyst-free technique. *Appl. Phys. A-Mater. Sci. Process.* **2022**, *128*, 99. [CrossRef]
45. Park, H.; Sen, A.; Kaniselvan, M.; AlMutairi, A.; Bala, A.; Lee, L.P.; Yoon, Y.; Kim, S. A Wafer-Scale Nanoporous 2D Active Pixel Image Sensor Matrix with High Uniformity, High Sensitivity, and Rapid Switching. *Adv. Mater.* **2023**, *35*, 2210715. [CrossRef] [PubMed]

Disclaimer/Publisher's Note: The statements, opinions and data contained in all publications are solely those of the individual author(s) and contributor(s) and not of MDPI and/or the editor(s). MDPI and/or the editor(s) disclaim responsibility for any injury to people or property resulting from any ideas, methods, instructions or products referred to in the content.